

# Evolutionary PERC+ solar cell efficiency projection towards 24% evaluating shadow-mask-deposited poly-Si fingers below the Ag front contact as next improvement step

Thorsten Dullweber<sup>\*</sup>, Maximilian Stöhr, Christian Kruse, Felix Haase, Martin Rudolph<sup>1</sup>, Birgit Beier, Philip Jäger, Verena Mertens, Robby Peibst, Rolf Brendel

*Institute for Solar Energy Research Hamelin (ISFH), Am Ohrberg 1, 31860, Emmerthal, Germany*



## ARTICLE INFO

### Keywords:

PERC  
PERC+  
Carrier selective contacts  
POLO  
TOPCon  
Shadow mask  
a-Si fingers

## ABSTRACT

Monofacial PERC and bifacial PERC + solar cells have become the mainstream solar cell technology exhibiting conversion efficiencies around 22.5% in mass production. We determine a specific saturation current density  $J_0$ ,  $Ag = 1400 \text{ fA/cm}^2$  of the screen-printed Ag front contact. When weighted with the contact area fraction of 3.0% the Ag metal contacts contribute  $42 \text{ fA/cm}^2$  to the total  $J_{0,total} = 130 \text{ fA/cm}^2$  thereby being a main limitation of the  $V_{oc}$ . We investigate carrier selective poly-Si on oxide (POLO) fingers below the screen-printed Ag contacts of PERC + solar cells in order to minimize contact recombination. We name this solar cell PERC + POLO. Numerical simulations reveal that PERC + POLO cells exhibit an efficiency potential up to 24.1% which is 0.3%<sub>abs.</sub> higher compared to PERC + solar cells. In order to enable low-cost manufacturing of poly-Si fingers, we investigate for the first time the deposition of suitable a-Si fingers by plasma-enhanced chemical vapour deposition (PECVD) through a shadow mask in a vacuum chamber. We demonstrate a-Si fingers as narrow as 70 μm and as high as 250 nm. The parasitic deposition below the mask increases the a-Si finger width by less than 30 μm compared to the mask opening width. First test wafers demonstrate an implied  $V_{oc}$  up to 716 mV of PECVD a-Si layers which are crystallized and doped in a subsequent  $\text{POCl}_3$  diffusion. Applying this process sequence, PERC + POLO cells could be manufactured with the established industrial PERC + process only adding the PECVD deposition of a-Si fingers through a shadow mask.

## 1. Introduction

Monofacial Passivated Emitter and Rear Cells (PERC) and bifacial PERC + solar cells [1] have become the mainstream solar cell technology in the photovoltaics industry exhibiting conversion efficiencies in mass production in the range of 22.0%–22.5% and in pilot production up to 23.0% [2]. A simulation study suggests that up to 24%-efficient industrial PERC cells can be developed in the future [3]. In order to suppress Ag contact recombination this previous study assumed that a selective emitter with very deep doping profile below the Ag contacts can be obtained by a deep phosphorus diffusion followed by a selective etch back process. However, such a process combination is so far too expensive for industrial production and hence has not yet been adapted in mass production by PERC cell manufacturers. Instead, several solar cell manufacturers manufacture selective emitters by laser doping [4],

which however only slightly increases the phosphorus concentration at the surface of the emitter [5] which is not sufficiently deep to strongly reduce contact recombination. Another promising approach to higher industrial cell efficiencies are carrier selective contacts applying polycrystalline silicon (poly-Si) on thin interfacial oxide named POLO [6] or TOPCon [7] and their industrial solar cell variants, in particular PERPOLy [8], TOPCon [9] and monoPoly [10] solar cells. These solar cells demonstrate conversion efficiencies around 23.0% [10] applying production-type processing sequences. Nevertheless, the processing costs are substantially higher compared to PERC since TOPCon-like solar cells apply silver (Ag) contacts on both wafer sides thereby almost doubling the metallization costs compared to PERC [11]. Also the n-type Cz wafers used for TOPCon are still a bit more expensive than p-type wafers for PERC and the boron diffusion takes longer and hence has a lower throughput than a phosphorus diffusion [11]. These may be

\* Corresponding author.

E-mail address: [dullweber@isfh.de](mailto:dullweber@isfh.de) (T. Dullweber).

<sup>1</sup> Now with Leibniz-Institut für Oberflächenmodifizierung (IOM), Permoserstraße 15, 04318 Leipzig, Germany.

reasons why the PV industry has not yet adopted TOPCon, PERPoly, and monoPoly as mainstream technologies in multi GW<sub>p</sub> production volumes.

This paper shows that the conversion efficiency of today's industrial PERC and PERC + solar cells is mainly limited by charge carrier recombination at the Ag front contacts. We evaluate a solar cell design which we name PERC + POLO, where 70 µm wide poly-Si fingers below the Ag metal contacts should drastically reduce charge carrier recombination. Our numerical simulations demonstrate an efficiency potential of up to 24.1% for PERC + POLO solar cells assuming industrial process technologies. A very similar type of solar cell has been presented in 2018 by JinkoSolar and in 2019 by LONGi Solar with experimental conversion efficiencies of 23.9% [12] and 24.1% [13], respectively, both obtained in R&D. However, JinkoSolar and LONGi did not present any process technology information about the poly-Si finger formation of these solar cells. In this paper, we propose a very cost-efficient PERC + POLO manufacturing process, which applies the well-established PERC + process and adds only one additional process step which is the PECVD deposition of a-Si fingers through a shadow mask. In the past, shadow masks have been applied e.g. for the deposition of 20 µm narrow Al metal fingers for lab-type solar cells [14]. Also, Q-Cells [15] and later CSEM and Meyer Burger [16] used shadow masks for the PECVD deposition of around 250 µm wide amorphous silicon fingers for rear contacted IBC heterojunction solar cells. In this paper, we present for the first time the deposition of down to 70 µm narrow a-Si fingers by PECVD through a shadow mask with only 40 µm mask opening which proves the principal feasibility of this approach. On first test wafers we convert intrinsic PECVD a-Si layers to n-type poly-Si during a POCl<sub>3</sub> diffusion and demonstrate good  $iV_{oc}$  values up to 716 mV which approach the best literature values for such test structures [11,17].

This paper is an extended version of a paper [18] published at the 29th Photovoltaic Solar Energy Conference, Xi'an, China, 2019. We add a historic PERC saturation current density progress review, list all Quokka simulation input parameters and present for the first time a detailed analysis of the dependence of the a-Si finger width and height on the PECVD shadow mask opening width.

## 2. $J_0$ analysis of past, present, and future PERC and PERC + solar cells

In order to predict future technology developments, it is a common approach in semiconductor technology to try to extrapolate technology

trends from the past into the future as e.g. published regularly in the ITRPV Roadmap [19]. Fig. 1 a) shows the record efficiencies of industrial PERC solar cells from 2010 till 2019. The best PERC + cell efficiencies since their first publication in 2015 [1] are shown as well with comparable front side efficiencies as the monofacial PERC cells. As a reference, published efficiencies of full-area Al-BSF solar cells are shown which, however, phase out of industrial mass production in favour of PERC and PERC+. The R&D-type PERC + POLO cells of Jinko and LONGi with efficiencies around 24% [12,13] are included in Fig. 1 a) as well. Whereas a typical industrial Al-BSF solar cell in the year 2010 had an efficiency around 17.5%, today's industrial PERC and bifacial PERC + solar cells exhibit average conversion efficiencies around 22.5% in mass production approaching the record PERC efficiencies around 23% displayed in Fig. 1 a). This corresponds to an efficiency increase of industrial silicon solar cells of 5%<sub>abs.</sub> within 9 years and a quite constant efficiency learning rate of around 0.5%<sub>abs./year</sub> during the last decade. Fig. 1 b) shows the historic trend of open circuit voltages  $V_{oc}$  of Al-BSF, PERC, and PERC + solar cells, which increased from 625 mV in 2010 to 685 mV in 2019 thereby being a main contributor to the 5%<sub>abs.</sub> efficiency increase shown in Fig. 1 a). The PERC design increased the  $V_{oc}$  of Al-BSF cells by approx. 20 mV. Further  $V_{oc}$  increases of PERC cells mainly originated from improved emitter doping profiles and reduced Ag front contact area as explained later in Table 1. Due to their similar device structure, PERC and PERC + solar cells exhibit very similar  $V_{oc}$  values as can be seen in Fig. 1 b). Unfortunately, the  $V_{oc}$  values of the 24% efficient PERC + POLO cells have not been published but are simulated in Fig. 4 to be around 700 mV. The  $V_{oc}$  improvements together with reduced Ag front grid shadowing and improved rear optics of PERC also strongly increased the short circuit current density  $J_{sc}$  from 37 mA/cm<sup>2</sup> in 2010 [21] up to 41 mA/cm<sup>2</sup> in 2019 [2] which also significantly contributed to the increased conversion efficiency in Fig. 1 a).

Table 1 lists the most important technology improvements from typical Al-BSF cells in 2010 to typical monofacial PERC and bifacial PERC + cells in 2019 enabling the continuous efficiency and  $V_{oc}$  increase of industrial silicon solar cells as shown in Fig. 1. Since PERC and PERC + cells exhibit almost identical saturation current density  $J_0$  values due to their very similar device structure, we show their  $J_0$  values for 2019 in a combined column "2019 PERC/PERC+" in Table 1. The  $J_0$  values stated in Table 1 are either measured for industry-typical PERC and PERC + cells processed at ISFH or taken from the literature as indicated in the following paragraphs. We add two columns in Table 1 extrapolating the future  $J_0$  reduction and  $V_{oc}$  improvement potential for PERC+

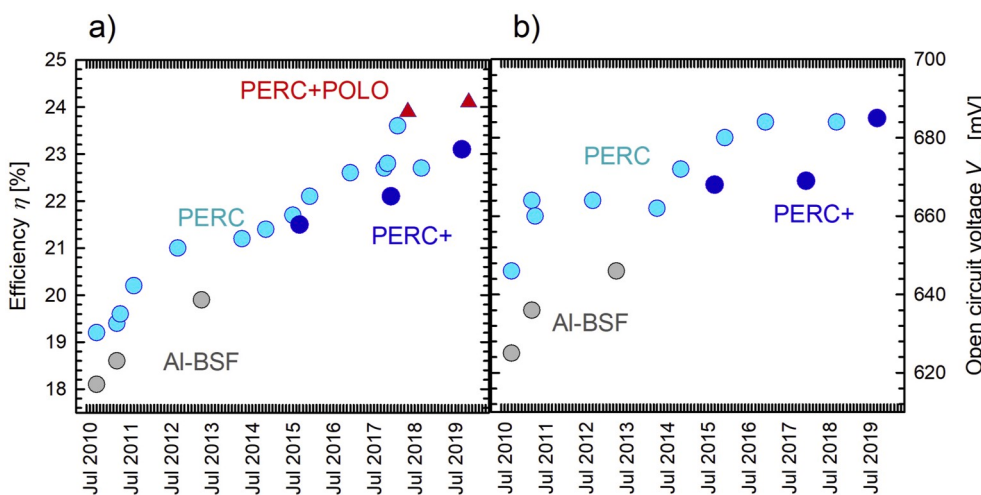


**Fig. 1.** a) The record efficiency (light blue dots) of industrial PERC solar cells has constantly increased by about 0.5%<sub>abs./year</sub> from 19.2% in 2010 up to 23.6% in 2019. The best bifacial PERC + cells (blue dots) exhibit similar efficiencies as the monofacial PERC cells. First R&D-type PERC + POLO cells shown as red triangles achieve efficiencies around 24%. b) The  $V_{oc}$  improved from 625 mV for Al-BSF cells (grey dots) in 2010 up to 685 mV for industrial PERC + cells in 2019 thereby being a main contributor to the increased conversion efficiencies. Unfortunately, the  $V_{oc}$  values of the record PERC + POLO cells have not been published but are simulated in Fig. 4. Fig. 2 and Table 1 explain the main reasons for the 5%<sub>abs.</sub> efficiency improvement during the past 9 years and provide a forecast for 2022. Fig. 1 is updated from Ref. [20] now also including Refs. [1,2,12,13,43]. (For interpretation of the references to colour in this figure legend, the reader is referred to the Web version of this article.)

a) PERC in 2011



b) PERC+ in 2019

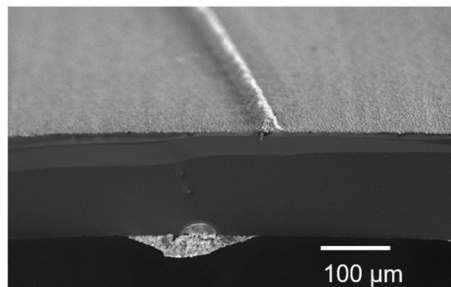


**Fig. 2.** Scanning electron microscopy (SEM) images of a) the 19.4%-efficient ISFH PERC record cell in 2011 (see Fig. 1) and b) a 22.3%-efficient ISFH bifacial PERC + solar cell from 2019. Whereas the Si wafer thickness remained constant at about 180  $\mu\text{m}$ , the Ag fingers widths has been reduced from around 100  $\mu\text{m}$  in 2010 down to around 35  $\mu\text{m}$  in 2019 minimizing light reflection and front contact recombination. The Al-BSF contact area fraction has been reduced from 100% for Al-BSF cells to around 10% for the early PERC cells in 2010 and to around 4% for today's PERC + solar cells. Whereas the y-axis is the same for both SEM images the x-axis of Fig. 2 a) is stretched by a factor 1.4 since the PERC cell has been broken in a 45° angle vs. the metal fingers. In Fig. 2 b), the cell has been broken with a 90° angle perpendicular to the Ag fingers.

**Table 1**

Detailed breakdown of the contributions to reducing the  $J_{0,\text{total}}$  from 578 fA/cm<sup>2</sup> in 2010 to 130 fA/cm<sup>2</sup> in 2019 which enabled a strong increase in  $V_{\text{oc}}$  as the main driver for the efficiency improvements in Fig. 1. Furthermore, a projection is provided for the expected  $J_0$  contributions of PERC+ and PERC + POLO cells in 2022 which are used in the Quokka simulations in Fig. 4. The individual  $J_0$  values have been either measured at ISFH or taken from the literature, see related text.

	2010 Al-BSF	Technology improvement	2019 PERC/ PERC+	2022 PERC+ POLO	2022 PERC + POLO
$f_{\text{Al}} \times J_{0,\text{Al-BSF}}$	100% x 300 fA/ $\text{cm}^2$	PERC	4% x 400 fA/ $\text{cm}^2$	1% x 400 fA/ $\text{cm}^2$	1% x 400 fA/ $\text{cm}^2$
$J_{0,\text{AlO}_x/\text{SiN}}$	n.a.	PERC	12 fA/ $\text{cm}^2$	1 fA/ $\text{cm}^2$	1 fA/cm <sup>2</sup>
$J_{0,\text{rear}}$	300 fA/ $\text{cm}^2$		28 fA/ $\text{cm}^2$	5 fA/ $\text{cm}^2$	5 fA/cm <sup>2</sup>
$J_{0,E}$	100 fA/ $\text{cm}^2$	In-situ/ex-situ Oxidation, LDSE	30 fA/ $\text{cm}^2$	22 fA/ $\text{cm}^2$	22 fA/ $\text{cm}^2$
$f_{\text{Ag}} \times J_{0,\text{Ag}}$	7% x 1400 fA/cm <sup>2</sup>	Fineline Ag print, OBB	3% x 1400 fA/ $\text{cm}^2$	2% x 1400 fA/cm <sup>2</sup>	2% x 35 fA/ $\text{cm}^2$
$J_{0,\text{front}}$	198 fA/ $\text{cm}^2$		72 fA/ $\text{cm}^2$	50 fA/ $\text{cm}^2$	23 fA/ $\text{cm}^2$
$J_{0,\text{bulk}}$	80 fA/ $\text{cm}^2$	low O <sub>b</sub> , Ga	30 fA/ $\text{cm}^2$	8 fA/ $\text{cm}^2$	8 fA/cm <sup>2</sup>
$J_{0,\text{total}}$	578 fA/ $\text{cm}^2$		130 fA/ $\text{cm}^2$	63 fA/ $\text{cm}^2$	36 fA/ $\text{cm}^2$
$\text{calc} V_{\text{oc}}$	636 mV		678 mV	696 mV	711 mV
$J_{\text{sc}}$	37.0 mA/ $\text{cm}^2$	PERC, fineline Ag print	41.0 mA/ $\text{cm}^2$	41.0 mA/cm <sup>2</sup>	41.0 mA/ $\text{cm}^2$
Bifaciality	0%	PERC+	80%	90%	90%

and PERC + POLO cells.

The key improvement when moving from Al-BSF cells to PERC cells was to reduce the area fraction  $f_{\text{Al}}$  of the aluminium rear contacts from 100% to around 4% today thereby drastically minimizing charge carrier recombination at the rear metal contact. Fig. 2 shows two SEM cross section images from a) a 19.4% efficient ISFH PERC cell in 2010 [21] and b) a 22.3% efficient ISFH PERC + cell in 2019. As can be seen, the early PERC cells had around 100  $\mu\text{m}$  wide line-shaped alloyed Al contacts which contacted around 10% of the rear area. By improving the laser contact opening pattern and the Al paste chemistry it was possible to further reduce the Al contact area fraction to around 4% while maintaining a well-alloyed aluminium back surface field (Al-BSF) enabling quite low  $J_{0,\text{Al-BSF}}$  values around 400 fA/cm<sup>2</sup>, as described in the review in Ref. 20 as well as according to ISFH internal measurements. Additionally, the Al fingers of PERC + cells limit the diffusion of Si into the Al paste during firing and hence may obtain slightly deeper Al-BSFs and lower  $J_{0,\text{Al-BSF}}$  values [22]. In any case, the specific  $J_{0,\text{Al-BSF}}$

= 400 fA/cm<sup>2</sup> of PERC and PERC+ is only slightly higher compared to full-area Al-BSF contacts with  $J_{0,\text{Al-BSF}}$  values around 300 fA/cm<sup>2</sup> [21]. Hence, the total area-weighted  $J_0$  contribution of the Al rear contacts reduced from 300 fA/cm<sup>2</sup> in 2010 to just 16 fA/cm<sup>2</sup> in 2019. In the next few years we expect that improved LCO geometries and Al pastes will further reduce the Al contact area fraction to around 1% without increasing the specific  $J_{0,\text{Al-BSF}}$  as already demonstrated in Ref. [23,24] thereby minimizing the area-weighted  $J_0$  contribution of the Al rear contacts to just 4 fA/cm<sup>2</sup> as shown in Table 1. At the same time, the AlO<sub>x</sub>/SiN<sub>y</sub> rear passivation covering almost 100% of the PERC + rear side contributes a  $J_{0,\text{AlO}_x/\text{SiN}}$  of only 12 fA/cm<sup>2</sup> to the total  $J_0$  [25] due to its excellent passivation properties. We expect that  $J_{0,\text{AlO}_x/\text{SiN}}$  will be reduced to 1 fA/cm<sup>2</sup> in the next few years by continuous process optimization as this value has been measured already at ISFH on test structures. Accordingly, the total rear side saturation current density  $J_0,\text{rear}$  which is the sum of the area weighted contributions of  $J_{0,\text{Al-BSF}}$  and  $J_{0,\text{AlO}_x/\text{SiN}}$  reduced from 300 fA/cm<sup>2</sup> in 2010 to 28 fA/cm<sup>2</sup> in 2019 and is expected to further reduce to just 5 fA/cm<sup>2</sup> in 2022.

Another important contribution to increased efficiency and  $V_{\text{oc}}$  was the reduction of the emitter saturation current density  $J_{0,E}$  from around 100 fA/cm<sup>2</sup> [26,27] back in 2010 to today's values around 30 fA/cm<sup>2</sup> [28,29] by developing advanced emitter doping profiles with reduced phosphorus surface concentrations applying techniques such as in-situ [30–32] and ex-situ oxidation [29,33]. The advanced diffusion processes reduce  $J_{0,E}$  while maintaining an emitter sheet resistance below 150  $\Omega/\text{sq}$ . which allows a wide spacing >1 mm of the Ag front contact fingers. As importantly were new developments such as improved Ag pastes and laser-doped selective emitters (LDSE) [4,5] which enabled to electrically contact the advanced doping profiles. We expect that this trend will continue and that  $J_{0,E}$  values of 22 fA/cm<sup>2</sup> will be applied in production in the next few years since such low  $J_{0,E}$  values have already been published in R&D [28,29].

One of the most important contributions to increased crystalline silicon solar cell conversion efficiencies in the past decades has been the continuous improvement of the front Ag pastes. Improved Ag paste chemistries enabled much narrower Ag finger widths [34] thereby reducing the optical shadowing loss and metal contact charge carrier recombination loss. Also, improved Ag pastes allowed to contact lightly doped emitters as stated above. The two SEM images in Fig. 2 demonstrate the huge progress in reducing the front Ag finger widths from approximately 100  $\mu\text{m}$  in 2010 to around 35  $\mu\text{m}$  in 2019 in accordance with Ref. 34. Accordingly, the metallization area fraction  $f_{\text{Ag}}$  of the Ag front fingers reduced from 5% in 2010 to around 2.5% in 2019. Simultaneously, the busbar design also changed during the past 9 years. Whereas in 2010 typically 3 busbars were printed with firing through Ag pastes contacting around 2% of the front surface, today's PERC + cells often apply non-firing through busbar pastes and/or advanced multi busbar designs [35] which cover less than 0.5% of the wafer front surface. Hence, the total contacted area fraction  $f_{\text{Ag}}$  (Ag fingers and busbars)

decreased from around 7% in 2010 to around 3% in 2019, see Table 1. For the front Ag contacts we determine a specific  $J_{0,Ag} = 1400 \text{ fA/cm}^2$  by a detailed carrier lifetime measurement and subsequent numerical modelling using Quokka. This value is within the range of previously reported  $J_{0,Ag}$  values from 200 to 2500  $\text{fA/cm}^2$  [33,36–38], which depend in particular on the sheet resistance and doping profile of the phosphorus emitter. Assuming a similar  $J_{0,Ag}$  of up to 1400  $\text{fA/cm}^2$  back in 2010, the area-weighted  $J_0$  contribution of the Ag front contacts reduced from 98  $\text{fA/cm}^2$  in 2010 to 42  $\text{fA/cm}^2$  in 2019 as stated in Table 1. We expect that it will be possible to further reduce the Ag finger width towards 25  $\mu\text{m}$  in the next years [34] hence further reducing the contacted area fraction  $f_{Ag}$  to 2% in 2022. However, it is quite challenging to reduce the high  $J_{0,Ag}$  of 1400  $\text{fA/cm}^2$ . One solution to suppress Ag contact recombination are selective emitters with very deep doping profile below the Ag contacts [33]. But the industry-typical laser-doped selective emitter forms only a shallow emitter since higher laser intensities required for deep doping melt the silicon pyramids [5]. Other techniques like deep phosphorus diffusion followed by a selective etch back process [26] are likely to be too expensive for industrial production and hence have not yet been adapted in mass production. Another promising approach to reduce metal contact recombination are carrier selective contacts applying polycrystalline silicon on thin interfacial oxide named POLO [6] or TOPCon [7] and their industrial solar cell variants. It has been shown that the carrier recombination at the screen-printed Ag metal contacts can be minimized to 35  $\text{fA/cm}^2$  by carrier selective poly-Si contacts [39]. When weighted with the contact area fraction of 2%, the recombination at the Ag/poly-Si contact is well below 1  $\text{fA/cm}^2$ . Hence, in Table 1 we introduce a column on the right named “PERC + POLO 2022” where we suggest to insert a poly-Si finger below the Ag finger of a PERC + solar cell similar to Ref. [12,13]. A schematic drawing of the PERC + POLO cell in comparison to an industry typical PERC + cell is shown in Fig. 3. The total front side saturation current density  $J_{0,front}$  which is the sum of the area weighted contributions of  $J_{0,Ag}$  and  $J_{0,E}$  reduced from 198  $\text{fA/cm}^2$  in 2010 to 72  $\text{fA/cm}^2$  in 2019 thereby being the main  $V_{oc}$  limitation of today's PERC and PERC + solar cells. We expect that advanced emitters and the PERC + POLO cell design will reduce  $J_{0,front}$  to 23  $\text{fA/cm}^2$  in 2022.

Finally, also the saturation current density  $J_{0,bulk}$  of the p-type Czochralski (Cz) silicon wafer material has been reduced from around 80  $\text{fA/cm}^2$  [40] in 2010 to around 30  $\text{fA/cm}^2$  in 2019 [41] by improving the wafer quality, reducing the oxygen content and by regeneration procedures minimizing boron oxygen defect recombination, see e.g. review in Ref. [42]. Here, we report  $J_{0,bulk}$  at a carrier density of  $1 \times 10^{15} \text{ cm}^{-3}$  which corresponds to  $V_{oc}$  conditions. The  $J_{0,bulk}$  values at maximum power point are slightly higher due to the injection dependence of the bulk carrier lifetime. In the past decade, the p-type Cz wafer resistivity decreased from around 2  $\Omega\text{cm}$  in 2010 to around 1  $\Omega\text{cm}$  in 2019 [41] which enables a wider Al finger spacing > 1 mm and hence increased bifaciality of PERC + solar cells. We expect that the improvement of the p-type Cz wafer material will continue and enable  $J_{0,bulk}$  values as low as 8  $\text{fA/cm}^2$  as evidenced by today's best R&D Cz wafers applying Ga

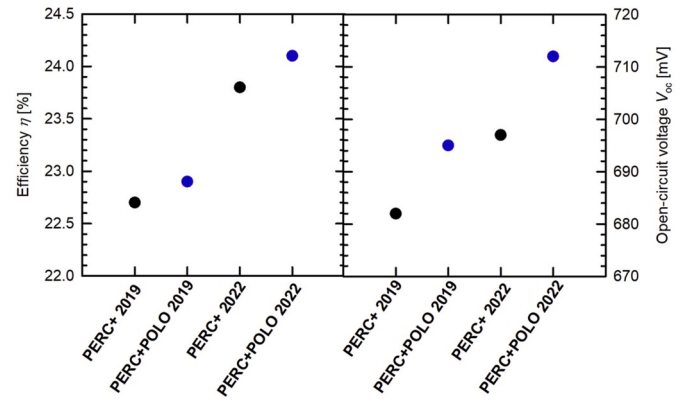


**Fig. 4.** Simulated conversion efficiency of PERC+ and PERC + POLO solar cells applying the software Quokka and typical PERC+ and POLO input parameters as measured in 2019 and as expected in 2022, see Tables 1 and 2. The application of POLO contacts increases the efficiency  $\eta$  by up to 0.3%<sub>abs.</sub> towards 24.1% and  $V_{oc}$  by up to 15 mV towards 712 mV.

doping or extremely low oxygen concentrations [41].

Adding up the individual area-weighted saturation current density contributions in Table 1 by applying the following equation (1) results in a total  $J_{0,total} = 578 \text{ fA/cm}^2$  for the Al-BSF cell in 2010.

$$J_{0,total} = f_{Ag} \times J_{0,Ag} + (1 - f_{Ag}) \times J_{0,E} + J_{0,bulk} + f_{Al} \times J_{0,Al} + (1 - f_{Al}) \times J_{0,Al} \quad (1)$$

$$V_{oc} = \frac{n k T}{q} \times \ln \left( \frac{J_{sc}}{J_{0,total}} \right) \quad (2)$$

When applying a one-diode model according to equation (2) with ideality factor  $n = 1$  and a short circuit current density  $J_{sc} = 37 \text{ mA/cm}^2$  [21], this  $J_{0,total}$  value corresponds to a  $V_{oc} = 636 \text{ mV}$  for the Al-BSF cell which fits well to measured IV parameters at that time [21]. For the PERC + cell in 2019, we obtain a  $J_{0,total}$  value of 130  $\text{fA/cm}^2$  corresponding to a  $V_{oc}$  of 678 mV when assuming  $J_{sc} = 41 \text{ mA/cm}^2$  [2]. This number is quite close to the  $V_{oc}$  of around 680 mV of today's typical PERC + cells [2]. Please note that the largest  $J_{0,total}$  contribution of 42  $\text{fA/cm}^2$  originates from the recombination at the Ag front contacts. Our extrapolation of the PERC + parameters to 2022 predicts a  $J_{0,total}$  value of 63  $\text{fA/cm}^2$  corresponding to a calculated  $V_{oc}$  of 696 mV which is limited, again, mainly by  $f_{Ag} \times J_{0,Ag} = 28 \text{ fA/cm}^2$ . Finally, the extrapolation to 2022 for the PERC + POLO cell results in the smallest  $J_{0,total}$  value of 36  $\text{fA/cm}^2$  corresponding to a calculated  $V_{oc}$  of 711 mV. Experimental evidence for this quite high calculated  $V_{oc}$  of PERC + POLO cells is given by measured implied open circuit voltages  $iV_{oc}$  up to 712 mV [29] of PERC + solar cells processed at ISFH without metal contacts which corresponds to a total  $J_{0,iVoc} = 35 \text{ fA/cm}^2$ . According to Table 1,  $iV_{oc}$  values of PERC + test structures differ from  $V_{oc}$  values of PERC + POLO cells mainly by the  $f_{Al} \times J_{0,Al-BSF}$  contribution which is

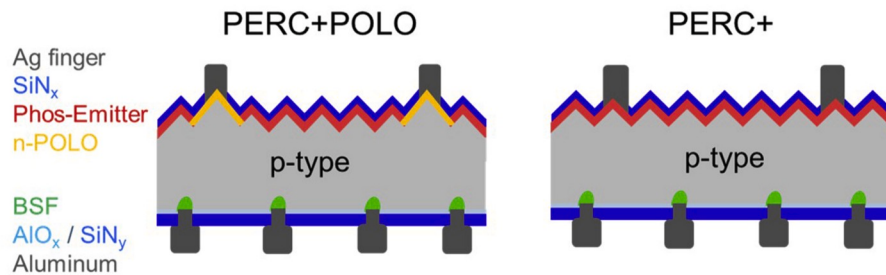


**Fig. 3.** Schematic drawings of PERC+ and PERC + POLO solar cells. The poly-Si on oxide (POLO) finger below the Ag finger drastically minimizes the front contact recombination.

only 4 fA/cm<sup>2</sup> in the 2022 scenarios. Since  $f_{Ag} \times J_{0,Ag}$  for PERC + POLO is < 1 fA/cm<sup>2</sup> and the  $f_{Al} \times J_{0,Al-BSF}$  is only 4 fA/cm<sup>2</sup>, it is expected that the  $J_{0,total}$  for PERC + POLO only increases by 5 fA/cm<sup>2</sup> from 31 to 36 fA/cm<sup>2</sup> after metallization and hence the cell  $V_{oc}$  for PERC + POLO will be close to the  $iV_{oc}$  of 712 mV [29] measured for the PERC + solar cells which corresponds to  $J_{0,iVoc}$  of 35 fA/cm<sup>2</sup> (assuming no  $J_0$  contributions from the additional Poly-Si process steps).

Another important improvement which significantly increases the energy yield of PERC solar cells and modules is the introduction of bifacial PERC solar cells named PERC+ [1] applying an Al finger grid on the rear side. Whereas the full-area Al-BSF cells in 2010 as well as the first commercial PERC cells were monofacial solar cells with 0% bifaciality, today's PERC + solar cells exhibit a bifaciality of up to 80% [1,2, 20]. Until 2022, we expect that the bifaciality of PERC + solar cells will increase up to 90% by further reducing the Al finger width in combination with multi busbar module designs as outlined in Ref. 43.

### 3. PERC + POLO Quokka simulations

We assess the conversion efficiency potential of PERC+ and PERC + POLO solar cells in detail with numerical simulations applying the conductive boundary model [44] as implemented in the software Quokka [45]. We simulate two "today" scenarios for PERC+ and PERC + POLO cells. The scenario "PERC+ 2019" uses all  $J_0$  and  $f$  parameters as stated in the column "2019 PERC/PERC+" in Table 1. The scenario "PERC + POLO 2019" also applies the  $J_0$  and  $f$  parameters as stated in the column "2019 PERC/PERC+" in Table 1 except for the  $J_{0,Ag}$  value where we use 35 fA/cm<sup>2</sup> for the Ag on POLO contact instead of 1400 fA/cm<sup>2</sup> for the Ag on phosphorus emitter contact. All other input parameters for both scenarios are given in Table 2 and have been measured at ISFH. The "PERC + POLO 2019" scenario assumes 90 µm wide poly-Si fingers in order to account for possible misalignment between poly-Si structuring and Ag screen printing. The optical absorption of the 90 µm wide poly-Si fingers is included in the PERC + POLO 2019 scenario using a ray-tracing approach with optical constants according to Refs. [46,47]. Table 3 lists the simulated current-voltage (IV) parameters of the "PERC+ 2019" scenario with a conversion efficiency  $\eta = 22.7\%$  which fits well to the industry status and to the PERC + cell in Table 3 processed at ISFH with  $\eta = 22.3\%$  efficiency measured in-house. As shown in Fig. 4, the "PERC + POLO 2019" simulation yields 0.2%<sub>abs.</sub> higher efficiencies and reaches 22.9%. The practically eliminated Ag contact recombination increases the  $V_{oc}$  from 682 mV for PERC + to 695 mV for PERC + POLO.

In a second set of simulations, we assume that within the next three years the PERC +  $J_0$  and  $f$  parameters will be further improved as stated in the column "2022 PERC+" of Table 1. Accordingly, the simulated "PERC+ 2022" efficiency increases to 23.8% and the  $V_{oc}$  to 697 mV. For the scenario "PERC + POLO 2022" we assume the  $J_0$  and  $f$  parameters as given in the column "2022 PERC + POLO" in Table 1, which are identical to "PERC+ in 2022" except for the much lower  $J_{0,Ag}$  value of the POLO contact. In addition, we assume that the poly-Si finger width can be reduced to 70 µm due to improved alignment between poly-Si structuring and Ag screen printing. Accordingly, the "PERC + POLO 2022" simulation achieves the highest conversion efficiency of 24.1%

**Table 2**

Input parameters used for the Quokka simulations in Fig. 4 as measured at ISFH. The  $J_0$  and  $f$  values of the different PERC+ and PERC + POLO scenarios were taken from Table 1.

Parameter	Value
Wafer resistivity	0.9 Ω cm
Wafer thickness	170 µm
Front contact shadowing	3.0%
Emitter sheet resistance $R_{sh}$	133 Ω/sq.
Specific contact resistance, front	1.5 mΩ cm <sup>2</sup>
Specific contact resistance, rear	1.3 mΩ cm <sup>2</sup>

**Table 3**

IV parameters of an industrial PERC + cell processed at ISFH in 2019 in comparison to the simulated scenarios "PERC+ 2019", "PERC+ 2022", and "PERC + POLO 2022" using the input parameters of Tables 1 and 2

	$\eta$ [%]	$V_{oc}$ [mV]	$J_{sc}$ [mA/cm <sup>2</sup> ]	FF [%]
ISFH PERC + cell	22.3	683	40.4	80.8
PERC+ 2019 Quokka	22.7	682	40.8	81.8
PERC+ 2022 Quokka	23.8	697	41.3	82.5
PERC + POLO 2022 Quokka	24.1	712	40.9	82.8

and the highest  $V_{oc}$  of 712 mV. Again, this high simulated  $V_{oc}$  is supported by our experimentally highest PERC + implied open circuit voltage  $iV_{oc}$  of 712 mV [29]. However, as shown in Table 3, the  $J_{sc}$  of the simulated PERC + POLO 2022 cell is 0.4 mA/cm<sup>2</sup> lower compared to the PERC+ 2022 cell due to absorption in the 70 µm poly Si fingers.

### 4. Proposed PERC + POLO manufacturing process by PECVD deposition of a-Si fingers through a shadow mask and subsequent crystallization

Since the efficiency gain of 0.3%<sub>abs.</sub> of PERC + POLO over PERC+ is relatively small, the poly-Si fingers have to be manufactured with as little additional costs as possible allowing only one or maximum two additional process steps compared to an industrial PERC + process in order to become economically attractive for a solar cell manufacturer. We propose a target process flow shown in Fig. 5 for the lean manufacturing of PERC + POLO solar cells by applying the well-established PERC + process steps inserting only one additional process step after texturing (1.), which is the plasma-enhanced chemical vapour deposition (PECVD) of amorphous Si (a-Si) fingers through a shadow mask (2.). The interfacial SiO<sub>2</sub> required for POLO or TOPCon can be either deposited wet chemically directly after texturing or by PECVD in-situ before the PECVD a-Si deposition [17]. Hence, we do not count the SiO<sub>2</sub> deposition as extra process step as it can be integrated into process step 1 or 2. The a-Si fingers are then crystallized to polycrystalline Si (poly-Si) and phosphorus-doped during the subsequent POCl<sub>3</sub> diffusion (3.). The PERC + POLO cells are completed by applying PERC + typical process steps such as (4.) front SiN<sub>y</sub> passivation, (5.) wet chemical rear polishing, (6.) AlO<sub>x</sub>/SiN<sub>y</sub> rear surface passivation, and (7.) rear laser contact opening, screen printing of rear Al and front Ag fingers, and

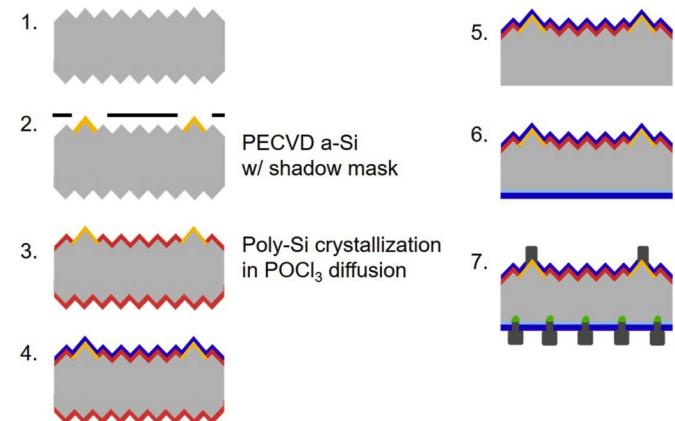


**Fig. 5.** Proposed target process flow for lean manufacturing of PERC + POLO solar cells by applying the well-established PERC + process steps only inserting one additional process step, which is the PECVD deposition of amorphous Si (a-Si) fingers though a shadow mask. The a-Si fingers are then crystallized to polycrystalline Si (poly-Si) and phosphorus-doped during the subsequent POCl<sub>3</sub> diffusion. The interfacial SiO<sub>2</sub> required for POLO or TOPCon can be either deposited wet chemically directly after texturing in step 1 or by PECVD in-situ before the PECVD a-Si deposition in step 2.

furnace firing.

As a first step towards the target process in Fig. 5, we investigate the deposition of a-Si fingers by PECVD through a shadow mask which is fixed on top of the silicon wafer by kapton tape in a vacuum chamber. The mask is aimed to be in proximity to the silicon wafer with a gap less than a millimetre. We use a lab-type deposition tool (Von Ardenne CS 400P) described in Ref. 48 applying an inductively coupled plasma (ICP) source that achieves a very high ionization rate and hence potentially very high deposition rates as demonstrated for  $\text{AlO}_x$  and  $\text{SiN}_y$  layers [48, 49]. As process gases we use 40 sccm of  $\text{SiH}_4$  and 160 sccm of  $\text{H}_2$  to deposit the intrinsic a-Si at a Si wafer heater set temperature of 300 °C. The deposition time is adjusted to obtain the desired a-Si film thickness, e.g. 90 s for 100 nm thickness. The Cz silicon wafers are transported on a substrate carrier. The shadow mask is placed on top of the silicon wafer and the a-Si is deposited from the top through the shadow mask on the Cz wafer as schematically illustrated in Fig. 5, process step 2. In accordance with the Quokka simulations we aim at a a-Si finger width in the range of 70 μm in order to minimize parasitic absorption in the poly-Si fingers. We target a-Si finger heights around 100 nm in order to avoid firing-through of the screen-printed Ag paste through the poly-Si layer.

In order to obtain the targeted a-Si finger properties, we evaluate the a-Si finger geometry in dependence of the mask opening line width. We apply a test mask which contains different finger opening widths of 40 μm, 60 μm, 80 μm, 120 μm, 150 μm up to 200 μm. Fig. 6 a) shows a 3 dimensional image measured with an optical profilometer (Wyko NT9100) of a 40 μm narrow and 250 nm high a-Si finger deposited through a 40 μm narrow mask opening on a polished float zone (Fz) wafer. Since the Fz wafer itself exhibits a surface roughness in the range of ±100 nm, it is very difficult to measure the exact a-Si finger profile, in particular the parasitic deposition of a-Si beyond the mask opening. Hence, we change the substrate to a glass substrate with a surface roughness below ± 5 nm. We then deposit a-Si fingers in one ICP PECVD a-Si deposition process with the process parameters as stated above applying the test mask with different line opening widths. We measure the a-Si finger geometries in dependence of the different mask opening widths with a mechanical profilometer (Dektak 150) shown as line scans in Fig. 6 b). To reduce statistical noise, each line scan in Fig. 6 b) has been averaged over 5 individual measurements. Both, the a-Si finger width as well as the finger height increase with increasing mask opening width. For each mask opening width, we determine the a-Si finger width at two different finger heights, namely the finger width at half maximum height (full width at half maximum = FWHM) as well as the finger width at the bottom of the finger close to the substrate. Fig. 7 a) plots both measured finger widths versus the mask opening widths. Whereas the FWHM a-Si finger widths are identical to the mask opening widths

confirming the 40 μm narrow a-Si finger of Fig. 6 a), the bottom finger widths are 20–30 μm wider than the mask opening widths revealing some parasitic deposition of a-Si below the shadow mask. Nevertheless, with 40 μm mask opening we obtain a bottom finger width of 70 μm which fits well to the assumptions in the Quokka simulations.

The a-Si finger height increases from 50 nm for 40 μm mask opening to 100 nm for 160 μm opening as displayed in Fig. 7b). For larger mask opening widths, the a-Si finger height remains constant at around 100 nm, which is identical to the a-Si layer thickness without mask. Hence, for our target mask opening width of 40 μm the finger height is reduced from 100 nm without mask to 50 nm with mask due to parasitic deposition of a-Si at the sidewalls of the mask. This corresponds to an a-Si material utilization of 50% when using 40 μm mask opening. As shown in Fig. 6 a) it is possible to obtain higher a-Si finger heights beyond our target value of 100 nm by increasing the deposition time of 90 s to higher values. In summary, the measured finger geometries with different test mask openings confirm that the target values (70 μm width, 100 nm height) can be obtained with 40 μm mask opening width and e.g. slightly increased deposition time.

We find these geometrical a-Si finger results quite encouraging and hence also study the conversion of a-Si to poly-Si according to Fig. 5, process step 3. In first experiments, we expose the ICP a-Si layers to a typical  $\text{POCl}_3$  diffusion (Centrotherm 2000 HT) and confirm by Raman measurements, that the a-Si layers crystallize to poly-Si layers similar as it has been demonstrated in Ref. 17 for PECVD a-Si layers. First symmetrically processed lifetime test structures applying damage etched, boron-doped Cz wafers with a resistivity of 1.1 Ωcm, a wet chemical interfacial oxide, full-area ICP a-Si layers, cleaning and a subsequent  $\text{POCl}_3$  diffusion demonstrate carrier lifetimes up to 609 μs corresponding to an implied  $V_{oc}$  up to 716 mV. The  $iV_{oc}$  corresponds to a total  $J_0 = 29 \text{ fA/cm}^2$  which allows to derive an upper limit for the n-type poly-Si layers of  $J_{0,poly} < 15 \text{ fA/cm}^2$ . However, very likely the  $J_0 = 29 \text{ fA/cm}^2$  is mainly limited by the wafer bulk carrier lifetime as similar  $J_0$  values have been obtained for this wafer material applying a high-quality  $\text{AlO}_x/\text{SiN}$  surface passivation. By further optimizing the ICP a-Si deposition,  $\text{POCl}_3$  diffusion, and wafer material we expect to improve the  $iV_{oc}$  values towards the present record values around 740 mV for PECVD a-Si layer which have been crystallized to n-type poly-Si [11, 17].

In the future we will apply the poly-Si fingers to PERC + POLO solar cells applying the target process flow in Fig. 5. In principle, the shadow mask deposition is relevant to any kind of solar cell structure which applies poly-Si fingers on the front or rear side, see e.g. the solar cell designs simulated in Ref. [50].

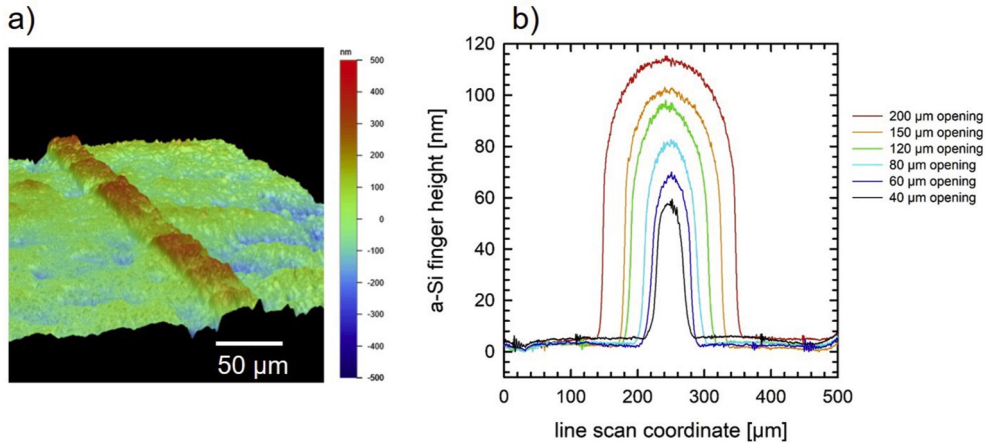


**Fig. 6.** a) Optical profilometer 3D-image of a 250 nm high and 40 μm narrow a-Si finger deposited by PECVD through a shadow mask on a polished float zone Si wafer. b) Line scans measured with a mechanical profilometer of a-Si fingers deposited through a shadow mask with different line openings ranging from 40 μm up to 200 μm opening widths on a glass substrate.

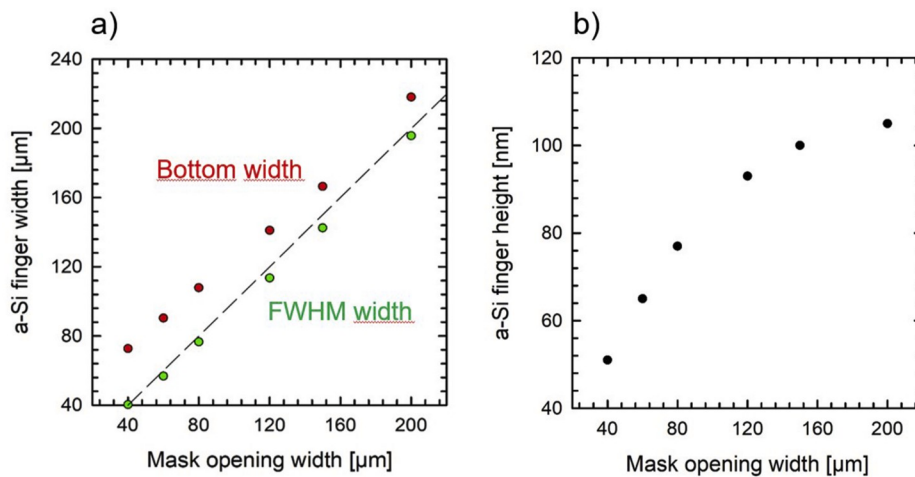


**Fig. 7.** Detailed analysis of the a-Si finger width and height in dependence of the mask opening width based on the line scans in Fig. 6 b). a) Measured a-Si finger widths at half-maximum finger height (FWHM width) and at the finger bottom (Bottom width) confirming that the a-Si finger width is mainly determined by the mask opening width. b) the a-Si finger height decreases with reduced mask opening width revealing some parasitic a-Si deposition at the mask sidewalls. In summary, the analysis shows that the a-Si finger target values (70  $\mu\text{m}$  width, 100 nm height) can be obtained with 40  $\mu\text{m}$  mask opening width and e.g. slightly increased deposition time.

## 5. Conclusion

In the past decade, almost all saturation current density  $J_0$  contributions of industrial silicon solar cells have been continuously reduced applying new process technologies such as the PERC concept with  $\text{AlO}_x/\text{SiN}_y$  rear passivation and LCOs, improved emitter doping profiles by in-situ and ex-situ oxidation, continuously improved Ag pastes enabling narrower Ag finger widths, and many others. The  $J_0$  reduction from around 578 fA/cm<sup>2</sup> in 2010 to around 100–150 fA/cm<sup>2</sup> today was a key contribution to increasing the conversion efficiency of 17.5% of Al-BSF cells in 2010 towards 22.5% of today's mass-produced PERC and PERC + solar cells.

The  $J_0$  analysis of present industrial PERC + solar cells reveals that the carrier recombination at the Ag front contact is the biggest contribution to the total  $J_{0,\text{total}}$  value thereby limiting the  $V_{oc}$  to below 700 mV. Hence, we evaluate the PERC + POLO cell concept which applies poly-Si fingers below the Ag contact thereby potentially minimizing the area-weighted  $J_{0,\text{Ag}}$  contribution to below 1 fA/cm<sup>2</sup>. Quokka simulations confirm that PERC + POLO cells obtain 15 mV higher  $V_{oc}$  values and up to 0.3%abs. higher conversion efficiencies compared to PERC + solar cells. When assuming further evolutionary improvements to PERC + POLO solar cells such as reduced emitter and wafer bulk  $J_0$  values, the Quokka simulation predicts that the conversion efficiency can be increased up to 24.1% with  $V_{oc}$  up to 712 mV. These simulations are supported experimentally by a measured implied open circuit voltage  $iV_{oc} = 712$  mV of PERC + cell precursors processed at ISFH without metal contacts as well as by the 24.1% efficient R&D-type PERC + POLO solar cell published by LONGi.

Due to the relatively small efficiency gain of PERC + POLO over PERC+, in order to be cost effective we propose a very lean manufacturing process flow for PERC + POLO which adds only one process step compared to PERC+, that is the local deposition of a-Si fingers by PECVD through a shadow mask. Applying an ICP plasma deposition process and varying mask opening widths, we find that the a-Si finger widths measured at half finger height (full width at half maximum, FWHM) match the mask opening widths very well enabling a FWHM a-Si finger width of 40  $\mu\text{m}$  with 40  $\mu\text{m}$  mask opening. However, the a-Si fingers slightly widen at the bottom by 20–30  $\mu\text{m}$  due to parasitic a-Si deposition below the mask hence leading to narrowest a-Si bottom finger widths of 70  $\mu\text{m}$ . With narrower mask opening widths, the a-Si finger height reduces by up to 50% compared to wide mask openings due to parasitic a-Si deposition at the sidewalls of the mask. Nevertheless, by increasing the deposition time we deposit up to 250 nm high a-Si fingers with FWHM width of 40  $\mu\text{m}$ . Accordingly, the test mask results confirm that the poly-Si finger width of 70  $\mu\text{m}$  and the poly-Si finger height of 100 nm assumed in the Quokka simulations can be

obtained by ICP a-Si deposition through a suitable shadow mask. First lifetime measurements reveal a good passivation property of ICP a-Si layers after  $\text{POCl}_3$  diffusion with  $iV_{oc}$  values up to 716 mV.

In the future, we will apply the ICP PECVD shadow mask deposition of a-Si fingers to PERC + POLO solar cells. Also, the mechanical stability of the mask during deposition, the mask and wafer handling in a possible future mass production application as well as the camera-based alignment of the screen-printed Ag fingers to the poly-Si fingers requires further research. Basically, the shadow mask deposition of a-Si fingers is relevant for any kind of solar cell design which applies poly-Si fingers on the front or rear side.

## Declaration of competing interest

The authors declare that they have no known competing financial interests or personal relationships that could have appeared to influence the work reported in this paper.

## CRediT authorship contribution statement

**Thorsten Dullweber:** Conceptualization, Writing - original draft, Supervision, Funding acquisition. **Maximilian Stöhr:** Methodology, Investigation, Formal analysis. **Christian Kruse:** Software, Validation. **Felix Haase:** Conceptualization, Methodology. **Martin Rudolph:** Methodology, Investigation, Project administration. **Birgit Beier:** Methodology. **Philip Jäger:** Investigation. **Verena Mertens:** Investigation. **Robby Peibst:** Conceptualization, Methodology. **Rolf Brendel:** Supervision.

## Acknowledgements

We gratefully acknowledge the support by the German Federal Ministry for Economic Affairs and Energy under the contracts 0324294C and 0324246B.

## Appendix A. Supplementary data

Supplementary data to this article can be found online at <https://doi.org/10.1016/j.solmat.2020.110586>.

## References

- [1] T. Dullweber, C. Kranz, R. Peibst, U. Baumann, H. Hannebauer, A. Füle, S. Steckemetz, T. Weber, M. Kutzer, M. Müller, G. Fischer, P. Palinginis, D. H. Neuhaus, PERC+: industrial PERC solar cells with rear Al grid enabling bifaciality and reduced Al paste consumption, Prog. Photovoltaics Res. Appl. 24 (2016) 1487–1498.

- [2] F. Stenzel, B.G. Lee, J. Cieslak, A. Schwabedissen, D. Wissen, S. Geißler, T. Rudolph, B. Faulwetter-Quandt, R. Hoenig, S. Wasmer, R. Bakowskie, D. Buß, F. Fertig, M. Schaper, A. Mette, J.W. Müller, Exceeding 23% and mass production of p-Cz Quantum bifacial solar cells, in: Proc. 36th Europ. Photovolt. Solar Energy Conf., 2019, pp. 96–99.
- [3] B. Min, M. Müller, H. Wagner, G. Fischer, R. Brendel, P.P. Altermatt, H. Neuhaus, A roadmap toward 24% efficient PERC solar cells in industrial mass production, *IEEE J. Photovoltaics* 7 (2017) 1541–1550.
- [4] S.J. Eisele, T.C. Röder, J.R. Köhler, J.H. Werner, 18.9% efficient full area laser doped silicon solar cell, *Appl. Phys. Lett.* 95 (2009) 133501.
- [5] S. Lohmüller, E. Lohmüller, P. Saint-Cast, J.M. Greulich, J. Weber, S. Schmidt, A. Moldovan, A.A. Brand, T. Dannenberg, S. Mack, S. Wasmer, M. Demant, M. Linse, R. Ackermann, A. Wolf, R. Preit, Key aspects for fabrication of p-type Cz-Si PERC solar cells exceeding 22% conversion efficiency, in: Proc. 33rd Europ. Photovolt. Solar Energy Conf., 2017, pp. 406–412.
- [6] R. Brendel, T. Dullweber, R. Gogolin, H. Hannebauer, N.-P. Harder, J. Hensen, S. Kajari-Schröder, R. Peibst, J.H. Petermann, U. Römer, J. Schmidt, H. SchulteHuxel, V. Steckenreiter, Recent progress and options for future crystalline silicon solar cells, in: Proc. 28th Europ. Photovolt. Solar Energy Conf., 2013, pp. 676–690.
- [7] A. Richter, J. Benick, F. Feldmann, A. Fell, M. Hermle, S.W. Glunz, n-Type Si solar cells with passivating electron contact: identifying sources for efficiency limitations by wafer thickness and resistivity variation, *Sol. Energy Mat. Sol. Cell.* 173 (2017) 96–105.
- [8] M.K. Stodolny, M. Lenes, Y. Wu, G.J.M. Janssen, I.G. Romijn, J.R.M. Luchies, L.J. Geerligs, n-Type polysilicon passivating contact for industrial bifacial n-type solar cells, *Sol. Energy Mat. Sol. Cell.* 158 (2016) 24–28.
- [9] F. Feldmann, T. Fellmeth, B. Steinhauser, H. Nagel, D. Ourinson, S. Mack, E. Lohmüller, J.-I. Polzin, J. Benick, A. Richter, A. Moldovan, M. Bivour, F. Clement, J. Rentsch, M. Hermle, S.W. Glunz, Large area TOPCon cells realized by a PECVD tube process, in: Proc. 36th Europ. Photovolt. Solar Energy Conf., 2019, pp. 304–308.
- [10] N. Nandakumar, J. Rodriguez, T. Kluge, T. Große, L. Fondop, P. Padhamnath, N. Balaji, M. König, S. Duttagupta, Approaching 23% with large-area monoPoly cells using screen-printed and fired rear passivating contacts fabricated by inline PECVD, *Prog. Photovoltaics Res. Appl.* 27 (2019) 107–112.
- [11] W. Deng, X. An, H. Chen, F. Jiang, G. Xing, in: Proc. 36th Europ. Photovolt. Solar Energy Conf., 2019, pp. 259–261.
- [12] H. Jin, Presented at the International Photovoltaic Power Generation and Smart Energy Conference & Exhibition, SNEC 2018, Shanghai, China, 2018.
- [13] J. Fan, H. Zhu, S. Zhang, H. Tong, H. Li, The roadmap to > 24% of PERC, Proc. 29th Photovolt. Sci. Eng. Conf. (2019) 1444–1446.
- [14] R. Hezel, Recent progress in MIS solar cells, *Prog. Photovoltaics Res. Appl.* 5 (1997) 109–120.
- [15] M. Scherif, Novel method for preparation of interdigitated back contacted a-Si:H/c-Si heterojunction solar cells, in: Proc. 26th Europ. Photovolt. Solar Energy Conf., 2011, pp. 2125–2129.
- [16] D. Lachenal, P. Papet, B. Legradic, R. Kramer, T. Kössler, L. Andreeta, N. Holm, W. Frammelberger, D.L. Baetzner, B. Strahm, L.L. Senaud, J.W. Schütttauf, A. Descoeuilles, G. Christmann, S. Nicolay, M. Despeisse, B. Paviet-Salomon, C. Ballif, Optimization of tunnel-junction IBC solar cells based on a series resistance model, *Sol. Energy Mat. Sol. Cell.* 200 (2019) 110036.
- [17] T. Gao, Q. Yang, X. Guo, Y. Huang, Z. Zhang, Z. Wang, M. Liao, C. Shou, Y. Zeng, B. Yan, G. Hou, X. Zhang, Y. Zhao, J. Ye, An industrially viable TOPCon structure with both ultra-thin SiO<sub>x</sub> and n+-poly-Si processed by PECVD for p-type c-Si solar cells, *Sol. Energy Mat. Sol. Cell.* 200 (2019) 109926.
- [18] T. Dullweber, M. Stöhr, C. Kruse, F. Haase, M. Rudolph, B. Beier, P. Jaeger, V. Mertens, R. Peibst, R. Brendel, PERC+POLO solar cells minimizing carrier recombination at the Ag front contact with simulated efficiency potential up to 23.8%, in: Proc. 29th Photovolt. Sci. Eng. Conf., 2019, pp. 1447–1451.
- [19] International Technology Roadmap for Photovoltaic (ITRPV.Net), 2018. Results, March 2019. Available at: <http://www.itrpv.net/Reports/Downloads/>.
- [20] T. Dullweber, High efficiency industrial PERC solar cells for monofacial and bifacial applications, in: V. Petrova-Koch, R. Hezel, A. Goetzberger (Eds.), High-efficient Low-Cost Photovoltaics, Springer Nature Switzerland AG, 2020, pp. 65–94.
- [21] T. Dullweber, S. Gatz, H. Hannebauer, T. Falcon, R. Hesse, J. Schmidt, R. Brendel, Towards 20% efficient large-area screen-printed rear-passivated silicon solar cells, *Prog. Photovoltaics Res. Appl.* 20 (2012) 630–638.
- [22] C. Kranz, U. Baumann, B. Wolpensinger, F. Lottspeich, M. Müller, P. Palinginis, R. Brendel, T. Dullweber, Void formation in screen-printed local aluminum contacts modeled by surface energy minimization, *Sol. Energy Mater. Sol. Cells* 158 (2016) 11–18.
- [23] Z.W. Peng, T. Buck, L.J. Koduvvelikulathu, V.D. Mihailescu, R. Kopecek, Industrial screen-printed n-PERT-RJ solar cells: efficiencies beyond 22% and open-circuit voltages approaching 700 mV, *IEEE J. Photovoltaics* 9 (2019) 1166–1174.
- [24] K. Tsuji, S. Suzuki, N. Morishita, T. Kuroki, M. Nakahara, M. Dhamrin, Z.W. Peng, T. Buck, N. Usami, Fine line Al printing on narrow point contact opening for front side metallization, *AIP Con Proc* 2147 (2019), 040019.
- [25] C. Kranz, S. Wyczanowski, S. Dorn, K. Weise, C. Klein, K. Bothe, T. Dullweber, R. Brendel, Impact of the rear surface roughness on industrial-type PERC solar cells, in: Proc. 27th Europ. Photovolt. Solar Energy Conf., 2012, pp. 557–560.
- [26] G. Hahn, Status of selective emitter technology, in: Proc. 25th Europ. Photovolt. Solar Energy Conf., 2010, pp. 1091–1096.
- [27] T. Dullweber, R. Hesse, V. Bhosle, C. Dubé, Ion-implanted PERC solar cells with Al2O3/SiNx rear passivation, *Energy Procedia* 38 (2013) 430–435.
- [28] W. Deng, F. Ye, R. Liu, Y. Li, H. Chen, Z. Xiong, Y. Yang, Y. Chen, Y. Wang, P. P. Altermatt, Z. Feng, P.J. Verlinden, 22.61% efficient fully screen printed PERC solar cell, Proc. 44th IEEE Photovoltaic Special Conf (PVSC) (2017), <https://doi.org/10.1109/PVSC.2017.8366416>.
- [29] P. Jäger, U. Baumann, T. Dullweber, Impact of the thermal budget of the emitter formation on the pFF of PERC+ solar cells, *AIP Con Proc* 2147 (2019) 140005.
- [30] A. Kimmerle, R. Woehl, A. Wolf, D. Biro, Simplified front surface field formation for back contacted silicon solar cells, *Energy Procedia* 38 (2013) 278–282.
- [31] A. Piechulla, S. Denzer, V.D. Mihailescu, T. Zhou, W. Joob, S. Eisert, R. Harney, Low pressure diffusions for high quality emitter formation in advanced p- and n-type solar cells, in: Proc. 31st Europ. Photovolt. Solar Energy Conf., 2015, pp. 420–424.
- [32] T. Dullweber, H. Hannebauer, S. Dorn, S. Schimanke, A. Merkle, C. Hampe, R. Brendel, Emitter saturation current densities of 22 fA/cm<sup>2</sup> applied to industrial PERC solar cells approaching 22% conversion efficiency, *Prog. Photovoltaics Res. Appl.* 25 (2017) 509–514.
- [33] A. Cuevas, P.A. Basore, G. Giroult-Matlakowski, C. Dubois, Surface recombination velocity of highly doped n-type silicon, *J. Appl. Phys.* 80 (1996) 3370–3375.
- [34] A. Lorenz, M. Linse, H. Frintrup, M. Jeitler, A. Mette, M. Lehner, R. Greutmann, H. Brocker, M. König, D. Erath, F. Clement, Screen printed thick film metallization of silicon solar cells – recent developments and future perspectives, in: Proc. 35th Europ. Photovolt. Solar Energy Conf., 2018, pp. 819–824.
- [35] S. Braun, G. Hahn, R. Nissler, C. Pönisch, D. Habermann, The multi-busbar design: an overview, *Energy Procedia* 43 (2013) 86–92.
- [36] H. Hannebauer, M. Sommerfeld, J. Müller, T. Dullweber, R. Brendel, Analysis of the emitter saturation current density of industrial type silver screen-printed front contacts, in: Proc. 27th Europ. Photovolt. Solar Energy Conf., 2012, pp. 1360–1363.
- [37] F. Ye, W. Deng, W. Guo, R. Liu, D. Chen, Y. Chen, Y. Yang, N. Yuan, J. Ding, Z. Feng, P.P. Altermatt, P.J. Verlinden, 22.13% efficient industrial p-type mono PERC solar cell, Proc. 43rd IEEE Photovoltaic Special Conf (2016), <https://doi.org/10.1109/PVSC.2016.7750289>.
- [38] V. Shanmugam, A. Khanna, P.K. Basu, A.G. Aberle, T. Mueller, J. Wong, Impact of the phosphorus emitter doping profile on metal contact recombination of silicon wafer solar cells, *Sol. Energy Mat. Sol. Cell.* 147 (2016) 171–176.
- [39] P. Padhamnath, J. Wong, B. Nagarajan, J.K. Batatis, L.M. Ortega, N. Nandakumar, A. Khanna, V. Shanmugam, S. Duttagupta, Metal contact recombination in monoPoly™ solar cells with screen-printed & fire-through contacts, *Sol. Energy Mat. Sol. Cell.* 192 (2019) 109–116.
- [40] T. Dullweber, C. Kranz, U. Baumann, R. Hesse, D. Walter, J. Schmidt, P. Altermatt, R. Brendel, Silicon wafer material options for highly efficient p-type PERC solar cells Proc, in: 39th IEEE Photovoltaic Specialists Conference, 2013, pp. 3074–3078.
- [41] B. Lim, A. Merkle, R. Peibst, T. Dullweber, Y. Wang, R. Zhou, LiD-free PERC+ cells with stable efficiencies up to 22.1%, in: Proc. 35th Europ. Photovolt. Solar Energy Conference, 2018, pp. 359–365.
- [42] T. Dullweber, J. Schmidt, Industrial silicon solar cells applying the Passivated Emitter and Rear Cell (PERC) concept—a review, *IEEE J. Photovoltaics* 6 (2016) 1366–1381.
- [43] T. Dullweber, H. Schulte-Huxel, S. Blankemeyer, H. Hannebauer, S. Schimanke, U. Baumann, R. Witteck, R. Peibst, M. Köntges, R. Brendel, Y. Yao, Present status and future perspectives of bifacial PERC+ solar cells and modules, *Jpn. J. Appl. Phys.* 57 (2018), 08RA01.
- [44] R. Brendel, Modeling solar cells with the dopant-diffused layers treated as conductive boundaries, *Prog. Photovoltaics Res. Appl.* 20 (2012) 31–43.
- [45] A. Fell, A free and fast three-dimensional/two-dimensional solar cell simulator featuring conductive boundary and quasi-neutrality approximations, *IEEE Trans. Electron. Dev.* 60 (2013) 733–738.
- [46] S. Reiter, N. Koper, R. Reineke-Koch, Y. Larionova, M. Turcu, J. Krügener, D. Tetzlaff, T. Wietler, U. Höhne, J.-D. Kähler, R. Brendel, R. Peibst, Parasitic absorption in polycrystalline Si-layers for carrier-selective front junctions, *Energy Procedia* 92 (2016) 199–204.
- [47] B. Min, M.R. Vogt, T. Wietler, R. Reineke-Koch, B. Wolpensinger, E. Köhnen, D. Tetzlaff, C. Schinke, R. Brendel, R. Peibst, Increasing the photo-generated current in solar cells with passivating contacts by reducing the poly-Si deposition temperature, *AIP Conf. Proc.* 1999 (2018), 040015.
- [48] T. Dullweber, C. Kranz, B. Beier, B. Veith, J. Schmidt, B.F.P. Roos, O. Hohn, T. Dippell, R. Brendel, Inductively coupled plasma chemical vapour deposited AlOx/SiNy layer stacks for applications in high-efficiency industrial-type silicon solar cells, *Sol. Energy Mat. Sol. Cell.* 112 (2013) 196–201.
- [49] B.F.P. Roos, O. Hohn, T. Dippell, B. Cord, M.R. Huber, P. Binkowska, Singular – a novel static inline PECVD-deposition concept for silicon cell production, in: Proc. 24th Europ. Photovolt. Solar Energy Conf., 2009, pp. 1665–1668.
- [50] R. Peibst, C. Kruse, S. Schäfer, V. Mertens, S. Bordihn, T. Dullweber, F. Haase, C. Hollemann, B. Lim, B. Min, R. Niepelt, H. Schulte-Huxel, R. Brendel, For none, one, or two polarities—how do POLO junctions fit best into industrial Si solar cells? *Prog. Photovoltaics Res. Appl.* (2019) <https://doi.org/10.1002/pip.3201>.